The interplay between calcite, amorphous calcium carbonate and intra-crystalline organics in sea urchin skeletal elements

Marie Alberic Alberic, Elad N Caspi, Mathieu Antoine Bennet, Widad Ajili, Nadine Nassif, Thierry Azaïs, Alex Berner, Peter Fratzl, Emil Zolotoyabko, Luca Bertinetti, et al.

The interplay between calcite, amorphous calcium carbonate and intra-crystalline organics in sea urchin skeletal elements

Marie Albéric[1], Elad N. Caspi[2], Mathieu Bennet[1], Widad Ajili[3], Nadine Nassif[3], Thierry Azaïs[3], Alex Berner[4], Peter Fratzl[1], Emil Zolotoyabko[4], Luca Bertinetti[1], Yael Politi[1*]*

[1]Department of Biomaterials, Max Planck Institute of Colloids and Interfaces, Potsdam 14476, Germany

[2]Physics Department, Nuclear Research Centre, Negev, P.O. Box 9001, Beer-Sheva 84190, Israel

[3] Sorbonne Universités, UPMC Univ Paris 06, CNRS, Collège de France, Laboratoire de Chimie de la Matière Condensée de Paris (LCMCP), Paris, France

[4]Department of Materials Science and Engineering, Technion-Israel Institute of Technology, 32000 Haifa, Israel

ABSTRACT

Biomineralization processes in living organisms result in the formation of skeletal elements with complex ultrastructures. Although the formation pathways in sea urchin larvae are known, the interrelation between calcite, amorphous calcium carbonate (ACC), and intra-crystalline organics in adult sea urchin biominerals is less clear. Here, we study this interplay in the spines and test

plates of the *Paracentrotus lividus* sea urchins whose skeletal elements have optimized function-properties relationships. Thermogravimetric analysis coupled with differential scanning calorimetry or mass spectrometry measurements, nuclear magnetic resonance technique and high-resolution powder X-ray diffraction show that pristine spines and test plates are composed of Mg-rich calcite and comprise about 10 wt. % of anhydrous ACC, 1.2 to 1.6 wt. % of organics, and less than 0.2 wt. % of water. Anhydrous ACC originates from incomplete crystallization of a precursor ACC phase during biomineralization and is associated with intra-crystalline organics at the molecular level. Molecular interactions at organic/inorganic interfaces cause significant calcite lattice distortions of the tensile type. The latter are amplified during ACC crystallization and finally disappear after heat-assisted destruction of organic molecules. Converting the measured lattice distortions (strains) into internal stress components, we follow stress evolution upon annealing and find that complete crystallization of ACC leads to the isotropy of residual stresses in all investigated skeletal parts. These results allow us to speculate that organic macromolecules are preferentially attached to different crystallographic planes in the pristine test and spine samples.

1. INTRODUCTION

Biogenic calcites are produced by a variety of marine organisms (e.g. algae, echinoderms, mollusks, etc.) and exhibit diverse crystal morphologies, sizes, and crystallographic orientations. They often have complex shapes and provide vital functions, such as mechanical reinforcement and optical filtering and focusing.[1-9] Sea urchins have different skeletal elements, among which, the coronal plates that form the test (body shell) and the spines that are projected from the test.

Although all these elements are calcium carbonate-based biominerals, their microstructures[10, 11] and magnesium contents are very different (2–12 mol% of Mg in spines[12, 13] and up to 11 mol% in the test plates[13, 14]). These variations are responsible for different mechanical properties[15, 16] of the skeletal parts that hence are adapted to specific functions.[17]

The test encases the internal organs of the sea urchins and protects them from the environment, whereas the spines are used for defense and locomotion. In order to further protect the test, the spines also function as sacrificial appendages that break easily and regenerate rapidly.[10, 18] Test plates and spines owe their lightweight material properties to a fenestrated porous meshwork, called the stereom differing in terms of geometry, regularity and density.[11] The main difference in terms of micromorphology between the test plates and the spines is that the former are only composed of stereom and the later also reveal external dense wedges called the septa (Figure 1). During spine formation, the stereom is first deposited and its pores are subsequently filled to form the septa.[10] The fenestrated stereom is likely responsible for the relative strength of the echinoid spines, as it can prevent crack propagation,[15] while the compact septa was shown to improve the bending stress resistance.[19]

Sea urchin skeletal elements also contain small amounts of intra-crystalline organics, defined as all organic molecules that are inserted into the mineral, in contrast to inter-crystalline organics, which separate individual mineral elements. During biomineralization, intra-crystalline organic molecules become occluded by growing mineral. The intra-crystalline organics is therefore protected by the mineral against chemical or biochemical digestion and can only be degraded by heat treatment.

In earlier works, the soluble and insoluble fractions of the intra-crystalline organic matrix were extracted from sea urchin skeletal elements, using different solutions (EDTA, HCl, acetic

acid).[20-22] The soluble protein fraction of *P. lividus* spines was determined to be 0.02 wt. %,[21, 23] while 0.1 wt.% of soluble and insoluble fractions were reported for *Arbacia lixula*.[22] Similarly, 0.2 wt. % of soluble and insoluble fractions were measured in the *P. lividus* test plates.[22] Proteins in sea urchin skeletal elements have been extensively characterized.[20, 21, 23] Besides some glycoproteins and monosaccharides have been identified[22, 24] and the presence of organic pigments was also reported.[20, 25]

Although sea urchin skeletal elements behave as single crystals in polarized light and X-ray diffraction,[26] they show conchoidal fracture-surfaces,[27, 28] which fundamentally differ from the atomically flat ones produced in geological calcite by cleavage. This behavior is attributed to impeded crack propagation by the occluded intra-crystalline organic molecules.[29] Organic molecules are attached to specific crystallographic planes and, hence, facilitate the formation of single crystals of different shapes (see e.g. brief review[30]). For example, it was shown that proteins in *P. lividus* sea urchin spines are preferentially adsorbed on calcite planes parallel to the *c*-axis (hk0-planes),[23] whereas proteins from sponge spicules and from calcitic prims of mollusk shells are mostly attached to the (001)-planes.[31-34] Note that in sea urchin spines, the *c*-axis is aligned with the long axis of the spines, whereas in the test plates (in *P. lividus* species), it is tangent to the test curvature in the apical direction.[35]

To provide single-crystal-like diffraction spots, the organic/inorganic interfaces have to be coherent, i.e. “invisible” by the diffracted X-rays. This takes place, if the distances between crystal unit cells along complex topologies, determined by organic macromolecules, can be expressed by an integer number of translation vectors.[36] However, atomic interactions at the interfaces may cause lattice distortions, as first detected in biogenic aragonite from *Acanthocardia tuberculata* bivalve shell[37] and thereafter in many other biogenic calcium

carbonate crystals (see, e.g. review[38]). Under mild annealing, the organic macromolecules are defragmented and removed from the bio-composite leading to the breaking of the interfacial coherence. This process is accompanied by the relaxation of lattice distortions and a substantial broadening of diffraction lines, indicating in turn a reduction in the size of crystalline blocks, which coherently scatter X-rays.[39]

Organic molecules are also known to stabilize amorphous precursor mineral phases and long-living amorphous phases.[40-43] The long-living amorphous calcium carbonate (ACC) phase present e.g. in calcareous sponges (ca. 15-20 wt.%) and in ascidians (ca. 80 wt.%) is hydrated.[44] In contrast, during the formation of sea urchin larval spicules, hydrated ACC is short-lived and transforms rapidly into a second disordered phase, most likely anhydrous transient ACC[45, 46] that slowly crystalizes into calcite. In adult sea urchin (*Anthocidaris crassispina*) spines, stable ACC (up to 8 at. %) was identified by nuclear resonance technique and suggested to be hydrated.[47] It was also evidenced that the inner stereom of sea urchin (*P. lividus*) spines is formed *via* an ACC phase,[48] whereas the crystallization of the septa was suggested to occur *via* direct crystallization without an ACC precursor phase.[19]

Sea urchin skeletal elements have been extensively studied,[21, 23, 29, 47, 49] but many questions still remain open, e.g. those regarding their composition and the interplay between components, namely calcite, ACC, and organic macromolecules. Here we address this issue by studying the spines and test plate samples annealed at different temperatures. The function of annealing is three-fold: water evaporation, crystallization of ACC and destruction of organic molecules. These transformations are monitored by thermogravimetric analysis (TGA) coupled with differential scanning calorimetry (DSC) or mass spectroscopy (MS) measurements. Highly accurate values of calcite lattice parameters, as well as total amount of non-crystalline

components at each temperature are extracted by applying Rietveld refinement to high resolution X-ray powder diffraction (HRXRD) data, collected at a dedicated synchrotron beam-line. In order to quantify the lattice distortions produced by intra-crystalline organics, one has to subtract the Mg-effect on lattice parameters, i.e. their decreasing with Mg concentration. For this purpose, Mg-content in different skeletal parts was determined by inductively coupled plasma optical emission spectrometry (ICP-OES) and wavelength-dispersive spectroscopy (WDS) in scanning electron microscopy (SEM). Such comprehensive characterization of chemical composition, phase content and differences in the atomic structure in different skeletal elements of a particular organism, *P. lividus*, contributes to our understanding of biomineralization pathways.

2. MATERIAL AND METHODS

2.1. Biogenic calcite samples

Sea urchins specimen of *P. lividus*, collected in the Atlantic Ocean, were received from the Roscoff marine station of Sorbonne University, University Pierre et Marie Curie (France) in June 2015. Large and small spines, as well as dissociated coronal plates of the test, were cut off three different sea urchins collected in the same place during the same period of the year. Small and large spines, being on average, respectively, 0.29±0.09 cm and 1.17±0.12 cm long, were taken from the same sea urchin specimens.

The samples were suspended in a 5% sodium hypochlorite (NaClO) solution for 5 h under agitation on a rocking table in order to remove the external organic material. After rinsing with distilled water and air-drying, the different skeletal elements were ground to produce fine

powders. The powders were further washed with NaClO for one day and then rinsed several times with distilled water and again washed with fresh NaClO for 12 h and rinsed.

The prismatic layers of the mollusk shells, *Pinna nobilis* (*P. nobilis*), collected in the Mediterranean Sea (Port-Cros Island, France) were used to produce fine powders studied for comparison. The powders were washed with NaClO for one day and then rinsed several times with distilled water.

2.2. Inductively coupled plasma - optical emission spectrometry (ICP-OES)

The total Mg-content in the spines and test plates was determined by ICP-OES (Optima 8000, Perkin Elmer Inc., USA) after dissolution of powdered samples in an acidic solution (167 μl HNO_3 and 333 μl HCl). The software WinLab 5.2 was used to extract and analyze the data.

2.3. Wavelength dispersive spectroscopy (WDS) in scanning electron microscopy (SEM)

Mg-concentration in large spines annealed at different temperatures was also measured by WDS in SEM. Measurements were carried out by using microscope FEI E-SEM Quanta 200 at the following experimental conditions: accelerating voltage - 30 kV, filament current - 55 nA, 30º take-off angle for collecting the fluorescent X-rays. For quantitative analysis with Ca Kα and Mg Kα X-ray lines, the diopside mineral ($MgCaSi_2O_6$) served as a lone standard. The coefficients of matrix correction were calculated for stoichiometric compositions of $Mg_xCa_{1-x}CO_3$. Using WDS, eleven samples were measured, in twenty sampling points each, the X-ray fluorescence signals being taken from central parts of visible mineral crystallites.

2.4. Thermogravimetric analysis (TGA) - differential scanning calorimetry (DSC) and TGA - mass spectrometry (MS)

TGA coupled with DSC measurements (SENSYS evo TGA-DSC, SETARAM Instrumentation, Caluire, France) were performed with approximately 30 mg of powdered samples placed in an aluminum or alumina crucible, depending on the maximum temperature to be reached in the experiment (500 or 820 °C, respectively). As we observed "jumping" of some powdered particles (mostly for large spines, Video SI) out of the crucible at about 450 °C, alumina caps were designed to cover the alumina crucibles in order to avoid any elusive weight loss due to this effect. Weight loss and heat flow were measured during programmed heating (25–820 °C at 2 °C/min, followed by holding at 820 °C for 30 min to 2 h), by using a nitrogen (20 mL/min) and oxygen (10 mL/min) purge gas mixture. Weight corrections for flow unbalances were made in order to accurately subtract the background and obtain reliable quantitative data for weight loss and heat flow.

For TGA coupled with MS measurements, we used LABSYS evo TGA-DSC, SETARAM system (France), combined with mass-spectra analyzer of gas discharge (QGA Hiden (UK)). These measurements were performed in the temperature range 25-600 °C at heating rate of 2 °C/min, using 20% O_2 in Ar, as purge gas mixture (30 ml/min).

2.5. Nuclear magnetic resonance (NMR)

NMR experiments were performed on a AV300 Bruker spectrometer operating at $\nu(^1H)$ = 300.29 MHz and $\nu(^{13}C)$ = 75.51 MHz. Zirconia rotors of 7 mm diameters were spun at a MAS frequency (ν_{MAS}) of 5 kHz. $\pi/2$ pulses were 4.7 and 3.5 μs for ^1H and ^{13}C, respectively. Recycle delays (RD) were set to 5 s for ^1H and $^1H \rightarrow ^{13}C$ cross polarization (CP) MAS experiments and

2000 s for ^{13}C single pulse experiments. For 1D $^{1}H \rightarrow ^{13}C$ CP MAS experiments, contact times of 250 μs, 500 μs, 1 ms and 10 ms were used. For 2D $\{^{1}H\}^{13}C$ HetCor experiments, the contact time was 1 ms and 48 t_1 increments of 400 scans were used. All ^{13}C spectra were proton decoupled at the acquisition (SPINAL 64). All spectra were referenced (δ = 0 ppm) to TMS for ^{1}H and ^{13}C.

2.6. X-ray diffraction

For high-resolution X-ray diffraction (HRXRD) measurements, fine powders of spines and test were prepared by grinding with mortar and pestle. The powders were then annealed for 1 h at selected temperatures: 50, 80, 100, 140, 170, 200, 250, 300, 350, and 400°C, in a Nabertherm 30-3000 °C oven equipped with a controller P320. About 20 wt.% of synthetic diamond powder (size $\leq 1\mu$m, 99.9% metals basis, Alfa Aesar 13401 LOT K222058), used as internal standard for X-ray diffraction measurements, was added to each one of the annealed sea urchin powders. Thus prepared samples were put in glass capillaries, 1 mm in diameter, and then measured at room temperature using high-resolution powder diffraction instrument at dedicated beam-line ID22 of European Synchrotron Radiation Facility (ESRF, Grenoble, France). The X-ray wavelength of 0.399952(2) Å was calibrated with Si standard sample (NIST, Gaithersburg, MD, USA). The use of the advanced analyzing optics resulted in diffraction patterns of superior quality and above all in intense and narrow diffraction peaks with an instrumental contribution to the peak widths not exceeding 0.004°[50]. Rietveld refinement of the obtained HRXRD profiles was performed with the FULLPROF package.[51]

Conventional X-ray diffraction (XRD) was used to check whether the decomposition of the initial $Mg_xCa_{1-x}CO_3$ into CaO and MgO is complete at high temperatures (about 820 °C). As

described below, this issue is important for estimating total amount of intra-crystalline organics and water in pristine samples. XRD measurements were performed using a laboratory X-ray diffractometer (Bruker D8, Germany), equipped with a standard sealed tube (Cu-anode, wavelength 1.5406 Å).

3. RESULTS

3.1. Skeletal elements morphology

Figure 1 shows the microstructure of the studied sea urchin skeletal elements. The coronal plates of the test (Figure 1A) are bearing large and small tubercles (Figure 1B), to which large and small spines are respectively anchored. The plates and tubercles are made of different types of stereom. The top of the tubercle is covered by a dense mineralized layer perforated with small pores (5 μm in diameter) irregularly arranged and the base is composed of a regular stereom with pores of about 10-15 μm in diameter connected by 5 μm-wide struts (Figure 1C). Fracture fragments reveal the stereom of the plate beneath (Figure 1C), which is more compact with smaller pores than the base of the tubercle.

Large and small spines consist of a base composed of stereom and a shaft (Figure 1G). Fractured cross-sections of the middle part of the shaft reveal dissimilar inner morphologies of large and small spines. They are both composed of a central laminar stereom with pores of 15-30 μm in diameter encircled by radial and longitudinal dense wedges (the septa) joined by galleried stereom (Figure 1H-L). However, in small spines, the septa is less developed and the stereom fraction larger than in large spines.

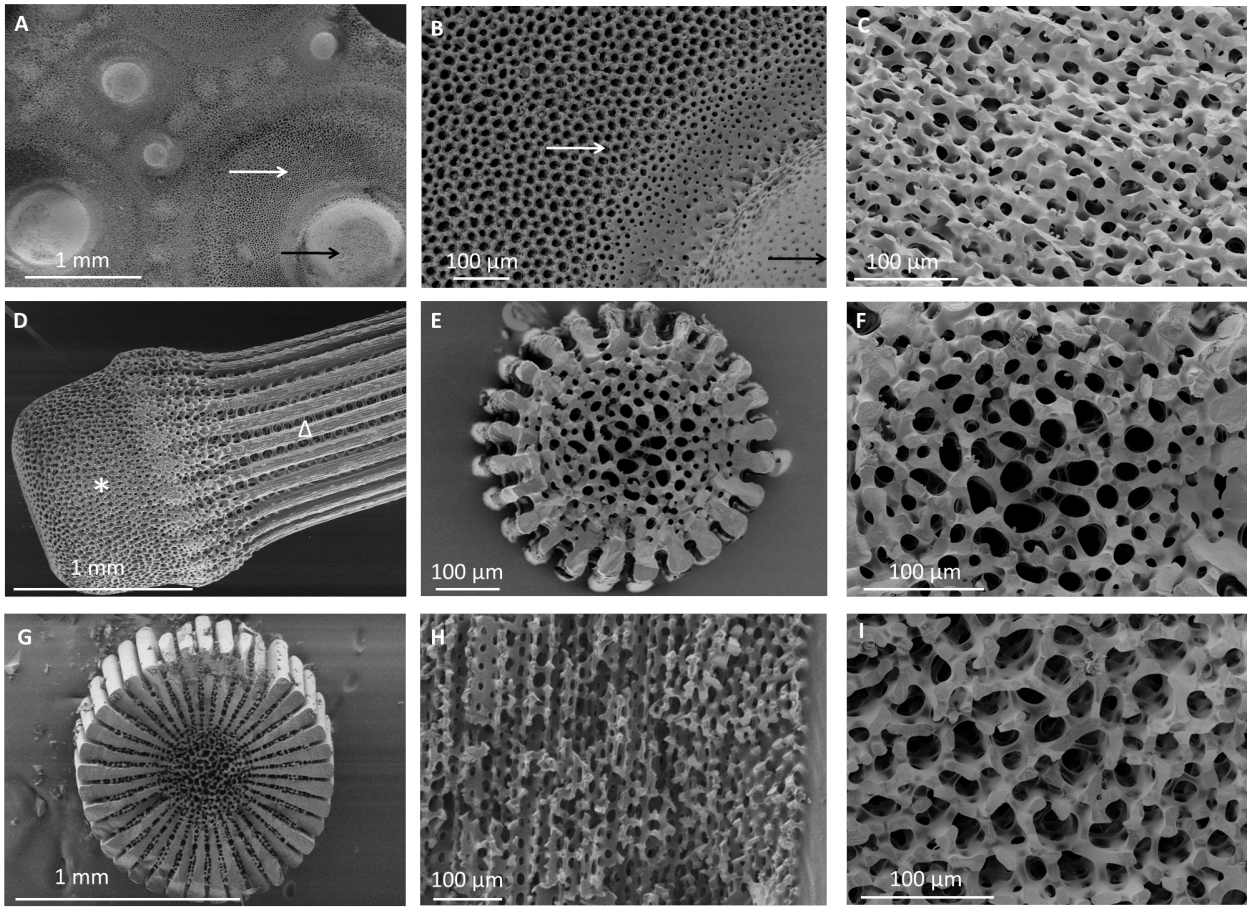

Figure 1: Scanning electron micrographs of the microstructure of sea urchin skeletal elements: A) coronal plates with the tubercles (top of the tubercle: black arrow, base of the tubercle: white arrow); B) high magnification of the tubercle; C) cross-section of the coronal plate, D) base (*) and shaft (Δ) of a small spine; E) cross-section of the middle of the shaft of a small spine perpendicular to its long axis; F) magnification of the inner stereom of E); G) cross-section of the middle of the shaft of a large spine perpendicular to its long axis; H) cross-section along the long axis of the spines; I) magnification of the inner stereom of G).

3.2. Mg content

The ICP-OES measurements of the Mg content, η (in percent), in $Mg_xCa_{1-x}CO_3$, $\eta = 100 \cdot x = 100 \cdot Mg/(Mg+Ca)$ yielded, 2.9 mol % for large spines, 3.6 mol % for small spines and 9.6 mol %

for the plates of the test. The η -value obtained in large spines by WDS, η = 2.96 mol % is close to that measured by ICP-OES.

3.3. TGA-DSC and TGA-MS analysis: organics, water, and ACC content

Using TG-DSC and TGA-MS measurements, we monitored the removal of water, the crystallization of ACC into calcite, and the combustion of organic macromolecules upon annealing and, on this basis, quantified their relative weight fractions in each skeletal element.

3.3.1. Weight fraction of intra-crystalline organics and water

In order to quantify the total amount of water and organics in pristine samples, TGA experiments were performed up to T = 820 °C (Figure 2A). At this temperature, $Mg_xCa_{1-x}CO_3$ is completely decomposed into CaO and MgO, as showed by XRD measurements (SI Figure 1). Based on the molar masses of Ca (M = 40.08 g/mol), C (M = 12 g/mol), O (M =16 g/mol), and Mg (M = 24.31 g/mol), and assuming that no organics and water remain after annealing at 820 °C, the weight fraction, ξ, of organics and water in pristine samples before annealing can be calculated depending on the Mg-concentration, x (molar fraction):

$$\xi = 1 - \frac{y}{(0.56-0.157x)}(1 - 0.157x) \qquad (1)$$

where y is the ratio between the weight of the final product (CaO+MgO) and the initial weight of the sample. This procedure yielded in average (with standard error of the mean) ξ = 1.8 ± 0.4 wt. % for the test plates, ξ = 1.4 ± 0.3 wt.% for the small spines and ξ = 1.5 ± 0.3 wt.% for the large spines. The water content determined by the TGA measurements up to 200 °C is very small (<

0.2 wt.%) in all samples (Figure 2A and B), as confirmed by MS measurements that did not record significant H_2O discharge up to 300 °C (SI Figure 2A). Thus, considering a maximum water content of 0.2 wt.% for all samples, the amounts of intra-crystalline organics in large spines, small spines and test plates are, respectively, 1.3 ± 0.2 wt.%, 1.2 ± 0.3 wt.% and 1.6 ± 0.4 wt.%. Therefore, these amounts are not significantly different in large and small spines, while slightly higher in test plates.

The derivatives of the TG-curves (dTG, Figure 2B) magnify the peculiarities of the weight loss, as a function of annealing temperature. The dTG of the large spines reveals the first weight loss region, with maximal loss rate at about 280 °C, corresponding to a weight loss of 0.9 ± 0.2 wt.% due to the destruction of organic macromolecules in agreement with CO_2 emissions at this temperature (SI Figure 2B). The second weight loss region, with maximal loss rate at about 450 °C, is due to further organics combustion accompanied by significant water and CO_2 emissions (SI Figure 2). At this temperature, the powder particles were observed to jump (jet effect) (see SI video), probably due to the explosion of gas-filled and water-filled inclusions as evidenced by the extensive gas discharge (SI Figure 2). This phenomenon resembles the process of rock decrepitation.[52, 53] The increase of the internal pressure in biogenic minerals was already estimated to be 200-350 MPa between 300 and 500 °C and suggested to be due to the destruction of organic macromolecules.[54]

Small spines show a dTG curve very similar to large spines, with first weight loss at about 280 °C (0.54 ± 0.1 wt.%) and the second one at 475°C (2.7 ± 0.2 wt.%). At the same time, the test plates reveal different dTG curve than those for large and small spines (Figure 2B). The first weight loss is smaller for the test plates than for the large spines (0.4 ± 0.1 wt.% versus 0.9 ± 0.2 wt.%, respectively) but it also correlates with CO_2 emissions and possibly with H_2O emissions.

The second weight loss region (350-600 °C) is composed of two distinct weight losses: one between 300 °C and 475 °C (1.5 ± 0.1 wt.%) and a second one between 475 °C and 600 °C (2.1 ± 0.3 wt.%) (Figure 2B). Interestingly, the decrepitation phenomenon was far less pronounced in the test plates than in the large spines (see SI video), suggesting that the internal pressure effect is less important for the former than for the latter. This is most likely due to the differences in microstructure. Specifically the presence of compact wedges in large sea urchin spines might prevent vapor and gas discharge whereas the presence of multiple micro-pore networks in test plates allows direct release of forming gas upon annealing.

For all samples, the second weight loss is higher than the total calculated organics content, based on measurements at 820 ºC. We attribute this difference to the partial overlap on the temperature scale between the combustion of intra-crystalline organics and early decomposition of the Mg-rich biogenic calcite (into CaO and MgO). Indeed, geological calcite begins to decompose at about 600 °C, whereas decomposition of the Mg-enriched calcite can start at about 400 °C[55, 56]; in addition, highly porous structures of sea urchins may facilitate the decomposition of biominerals at lower temperatures. Upon heating at 600 °C and above, all our samples show substantial mineral phase decomposition with a third massive weight loss and a significant CO_2 discharge (SI Figure 2).

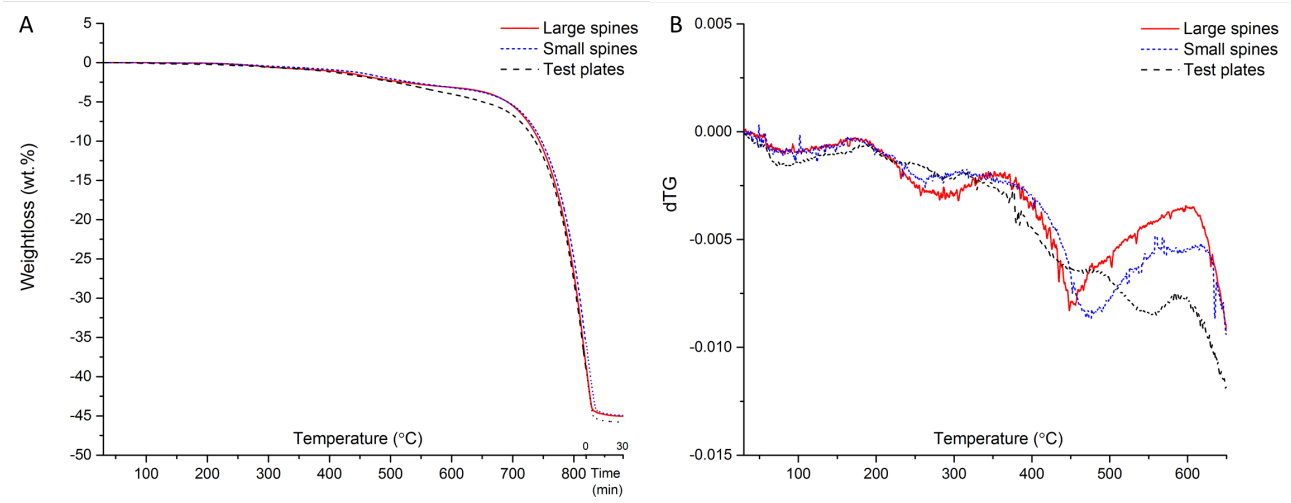

Figure 2: A) TG measurements in temperature range between room temperature and 820°C, followed by holding samples at the latter for 0.5 h; B) the corresponding derivatives of the TG-curves (dTG). Data for large spines, small spines, and test plate are colored, respectively, in red, blue, and black.

The heat flow measurements (Figure 3) revealed several exothermic peaks. The first peak is observed in all samples around 200 °C and is not accompanied by any significant weight loss. It is therefore assumed to be the result of ACC crystallization, as discussed in detail below. The second exothermic peak, at about 290 °C for large spines and at about 260 °C for small spines and test plates (Figure 3), is due to partial destruction of intra-crystalline organic molecules, which corresponds to the first weight loss region described above.

3.3.2. Crystallization of ACC

As mentioned above, the first exothermic peak at around 200 °C is related to the crystallization of the ACC fraction present in the skeletal elements, since no weight loss or significant gas discharge were detected around this temperature (Figures 2 and 3). Based on the heat flow

measurements, the weight fraction of ACC in pristine sea urchin skeletal elements can be estimated, as:

$$\Phi = \frac{\Delta H \cdot M}{\Delta H_{cr}} \qquad (2)$$

where ΔH is the total heat flow per gram of sample (the area under exothermic peak), ΔH_{cr} = 13 kJ/mol is the crystallization enthalpy of ACC,[57] and M the molar mass of $Mg_xCa_{1-x}CO_3$. The areas under the peaks were determined after baseline correction and peak fitting. This calculation yielded ACC weight fraction of Φ = 8 ± 1 wt.% for large spines, Φ = 10 ± 2 wt.% for small spines, and Φ = 10 ± 1 wt.% for test plates.

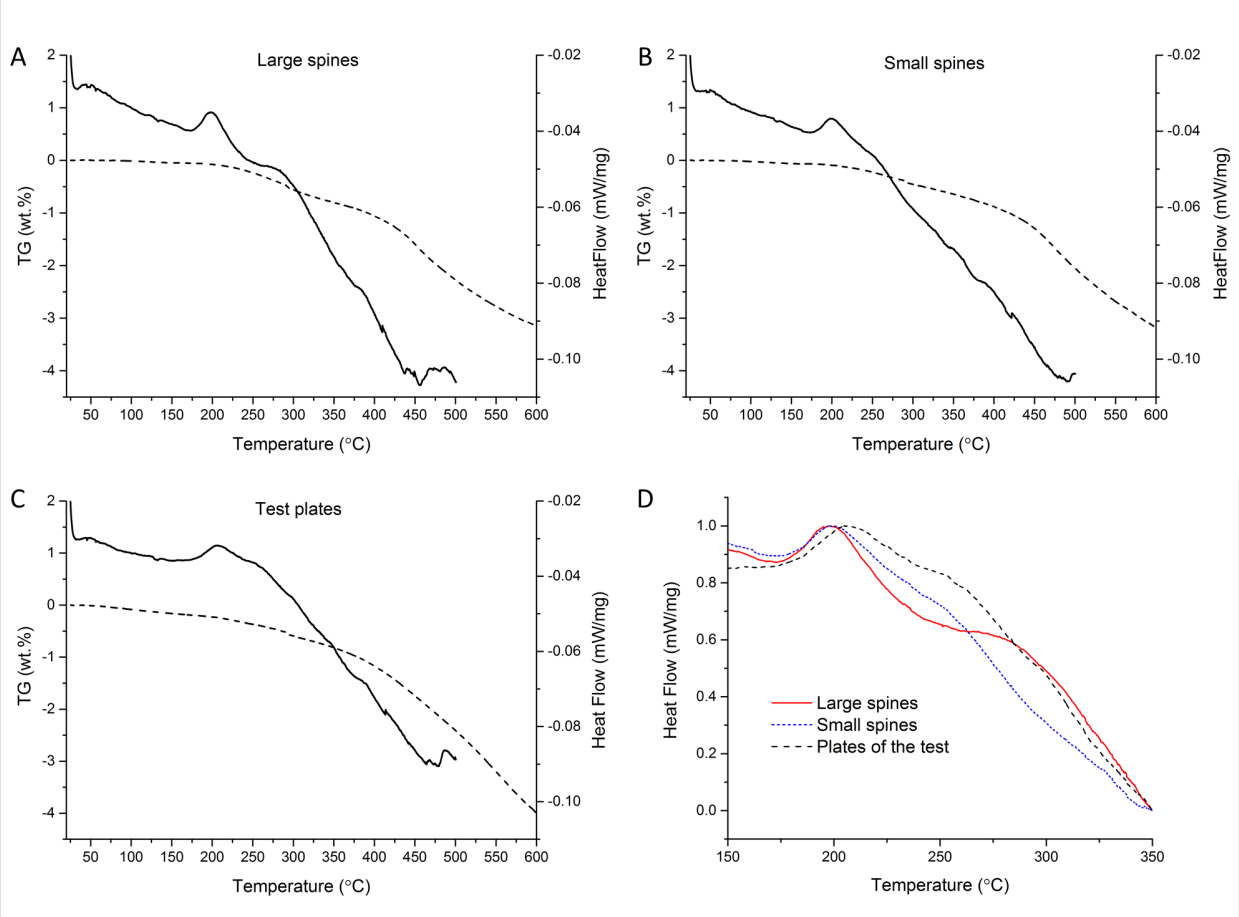

Figure 3: The results of TG-DSC measurements in: A) large spines; B) small spines; C) plates of the test. Dashed and solid lines show the TG and DSC results, respectively; D) normalized heat flow in large spines (red curve), small spines (blue curve), and test plates (black curve).

3.4. NMR analysis – the environment of water within the minerals

As expected, the single pulse ^{13}C MAS NMR spectrum (quantitative spectrum - fully relaxed) of the sea urchin large spines and test plates powdered samples display one single resonance at 168.4 ppm characteristic of calcite[58] and indicating that calcite is the only $CaCO_3$ polymorph present in these samples (Figure 4, ^{13}C quantitative red spectra and SI Figure 3A). Interestingly, we note that the full width at half maximum (FWHM) of the 168.4 ppm resonance is broader for the test plates (1.1 ppm) than for the large spines (0.6 ppm), indicating a higher local disorder in calcite from the test plates compared to the large spines. This difference in local order might be due to the different Mg concentration in the two samples[47], but also due to distinct amount and/or nature of the non-crystalline fractions (organics and ACC).

By performing ^{13}C cross polarization experiments ($^{1}H \rightarrow ^{13}C$ CP MAS), in which carbonates in a protonated environment are highlighted, we evidenced a slightly shifted (168.7 ppm for large spines and 168.6 ppm for test plates) and broader resonance (1.3 ppm for large spines and 1.6 ppm for test plates) with a Gaussian line shape characteristic of a disordered environment (Figure 4 and SI Figure 3B). This confirms the presence of ACC domains in both samples, as already proposed in sea urchin spines.[47]

The FWHM of the ACC ^{13}C resonance from sea urchin skeletal elements is twice smaller than the one reported for synthetic ACC[58, 59] and biogenic ACC gastrolith (enriched in P)[60, 61],

suggesting that ACC in mature sea urchin large spines and test plates is more ordered than stable biogenic ACC in crayfish [60] and lobster [61] gastrolith.

Furthermore, 2D $\{^1H\}^{13}C$ HetCor experiments (allowing the spatial correlation between ^{13}C carbonates resonances and ^1H signals from protonated species) reveal that carbonates from ACC of both samples are strongly bonded to water molecules (characteristic chemical shift $\delta(^1H)$ = 6 ppm[62]) (Figure 4). By varying the contact time (from 250 μs to 10 ms), neither variation in position nor in line width of the ^{13}C ACC-like resonance was observed (SI Figure 3C), suggesting that H_2O molecules are homogeneously distributed within the ACC domain. We note that no bicarbonates ions are present in ACCs (absence of the typical correlation resonance at $\delta(^1H)$ = 14 ppm[63]). Finally, due to similar ^{13}C resonances (chemical shifts and FWHM) and spatial correlations, ACC in plates and spines are very similar in terms of local structure.

The relatively low organics content determined by TGA (about 1.4 wt. % in average for all samples) does not result in a strong enough ^{13}C NMR signal (SI Figure 3B) and consequently no correlation between water molecules and organics were identified in 2D $\{^1H\}^{13}C$ HetCor experiments. Therefore, no proximity between water molecules and organics could be identified. If all the water content determined by TGA (0.2 wt. %) is assumed to be bond to ACC, ACC should have a $Ca:H_2O$ molar ratio of 1:0.1,which can be considered as relatively anhydrous.

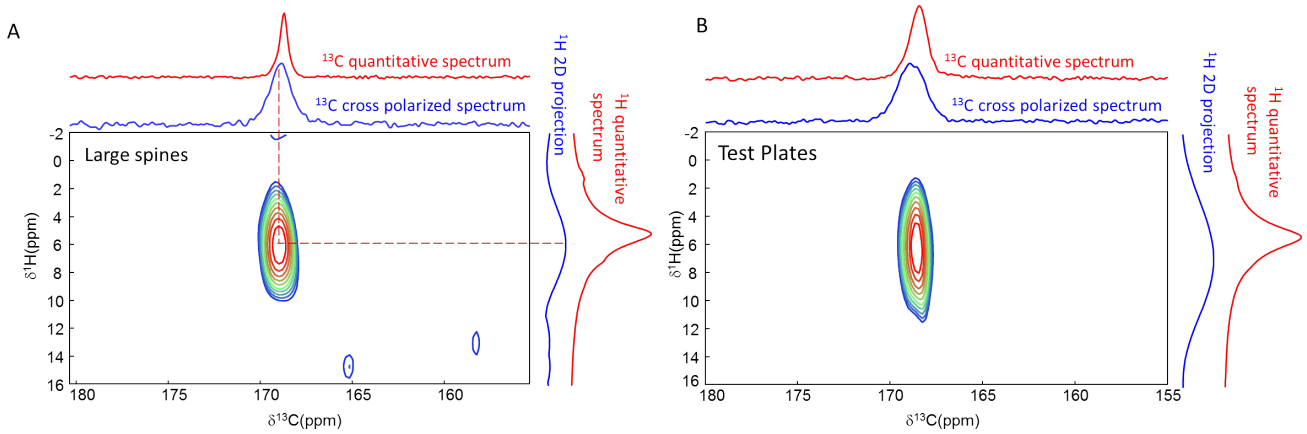

Figure 4: 2D {^{1}H}^{13}C HetCor spectrum of sea urchin skeletal element powdered samples of A) the large spines and B) the test plates with a recycle delay of 5s and a contact time of 1 ms. In blue, ^{13}C cross polarized spectrum and ^{1}H 2D projection and in red ^{13}C and ^{1}H quantitative spectrum.

3.5. High-resolution X-ray diffraction (HRXRD)

HRXRD combined with Rietveld refinement provides information on the structure of the investigated samples. Using an internal standard method it is also possible to quantify the amount of amorphous phase in the samples (see e.g.[64]). Here, we apply this technique for *ex-situ* characterization of sea urchin skeletal elements previously annealed at different temperatures. The HRXRD measurements of annealed powders were performed at room temperature in order to avoid thermal expansion effects on lattice parameters. HRXRD profiles revealed sharp diffraction peaks of $Mg_xCa_{1-x}CO_3$ and of the diamond powder added as internal standard (SI Figure 4). Diffraction profiles, taken from annealed samples, are very similar to that before annealing, with only some differences in in the angular distribution of the background intensity (SI Figure 4). Moreover, Rietveld refinements confirmed that at all annealing temperatures calcite has its conventional rhombohedral structure (space group # 167). Applying Rietveld

refinement yielded the lattice parameters, *a* and *c* (in hexagonal setting), as well as the diamond (D) powder weight fraction, β = D/(calcite + D), with respect to that of calcite (the latter after extinction corrections[61]).

3.5.1. Weight fraction of non-crystalline components

In the internal standard method used, the values of β extracted by Rietveld refinement are compared with the weight fraction of the diamond powder, γ = D/(calcite + D + A), directly measured (by weighting) during sample preparation. Here A denotes the amount of all non-crystalline components (ACC, water and organics) in our powdered samples. Based on these definitions, the weight fraction of the non-crystalline phases in the sample is given by the expression[64]:

$$\Psi = \frac{A}{calcite+A} = \frac{\beta-\gamma}{\beta(1-\gamma)} \qquad (3)$$

which is proportional to the difference, $(\beta - \gamma)$. The equality, $\beta = \gamma$, means a complete transformation of ACC to calcite and the removal of water and intra-crystalline organics.

The non-crystalline weight fractions, Ψ, are plotted for all three types of investigated samples, as functions of annealing temperature (Figure 5A). Despite the scattering of the obtained values and the rather large measurement errors (which are intrinsic to this method in the case of small amounts of amorphous phase), the two main trends are evident: (*i*) the non-crystalline fraction is maximal in pristine samples and is diminishing to zero with annealing temperature; (*ii*) the reduction of the magnitude of Ψ is most pronounced between 200 and 250 °C. These trends are clearly seen in Figure 5B in which the data averaged over the three different kinds of samples (small and large spines, as well the test plates) are plotted. Thus, pristine sea urchin samples contain on average of about 12 wt. % of non-crystalline components. After subtracting the

averaged organics and water contents, measured by TGA (totally, 1.6 wt. % see, section *3.3.1*), the average percentage of ACC is 10.4 wt. %. This number fits well the one obtained in DSC measurements in section *3.3.2*. Also the temperature range of the amorphous/crystalline phase transformation, 180 - 300 °C, in Figure 5B is in good agreement with the interval obtained in DSC measurements in section *3.3.2*.

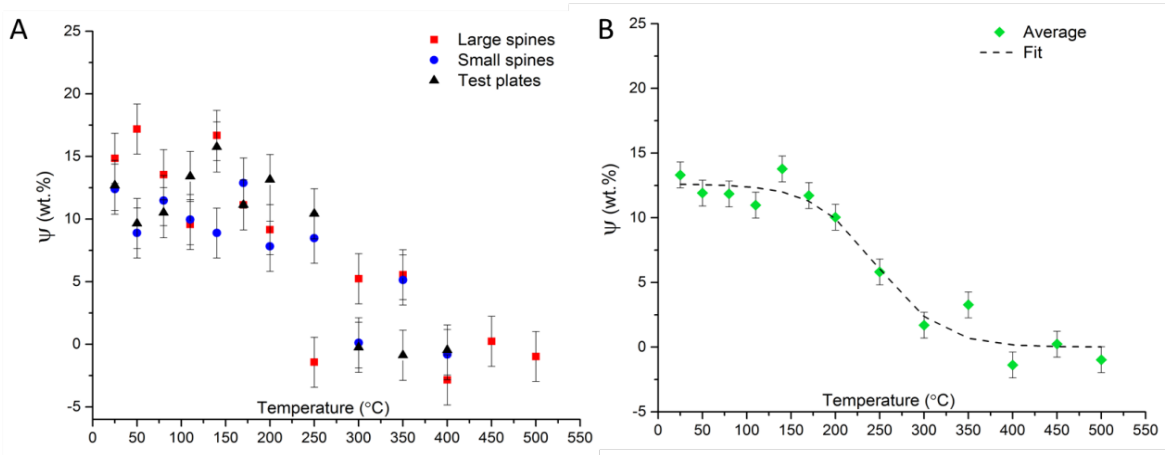

Figure 5: Temperature dependences of: A) the weight fractions of non-crystalline component, Ψ, in large spines, small spines, and test plates; B) the non-crystalline weight fraction averaged over three kinds of samples (green diamonds) and the best fit to the smooth-step function (dashed line).

3.5.2. Calcite lattice distortions in sea urchin elements

Lattice parameters in biogenic crystals are affected by the atomic interactions at the organic/inorganic interfaces and can provide important information on the latter.[38] HRXRD combined with Rietveld refinement is a powerful method used to extract highly accurate values of lattice parameters and their changes with respect to geological or synthetic crystals (in this case to geological calcite). Applying Rietveld refinement to high-resolution synchrotron diffraction data, we obtained excellent refinements of calcite structure for all pristine and

annealed samples with goodness of fit between χ^2 = 2.21–3.38 for large spines, χ^2 = 2.49–3.98 for small spines, and χ^2 = 1.61–3.38 for test plates.

The extracted lattice parameters, *a* and *c*, as well as the fractional coordinate, X (defining the oxygen atomic positions), for all annealing temperatures are summarized in SI - Table 1 (for large spines), SI - Table 2 (for small spines), and SI -Table 3 (for test plates). The lattice parameters, *a* and *c*, are also plotted as functions of annealing temperature, in Figures 6A and B, respectively. Both lattice parameters, *a* and *c*, show substantial reduction with increasing Mg-concentration in the series: large spines/ small spines /test plates. Besides, some peculiarities in the temperature dependences of lattice parameters are observed when calculating the lattice distortions with respect to geological calcite (Figures 6C and D).

In order to determine the net organics-induced lattice distortions in biogenic calcite, we first remove the Mg-contribution from the obtained lattice parameters. This is done using Mg-calibration curves[13] and the measured Mg concentrations in the spines and test samples (section *3.2*). The lattice distortions, $\Delta a/a$ and $\Delta c/c$, in sea urchin skeletal elements are plotted in Figures 6C and 6D, respectively, as functions of annealing temperature.

The lattice distortions, $\Delta a/a$, are small in all pristine skeletal elements studied ($\Delta a/a \approx$ 0.03–0.05 %), whereas the magnitude of $\Delta c/c$ is nearly 0.04 % in the spines and significantly higher ($\Delta c/c \approx 0.1\%$) in pristine test plates samples. These initial (before annealing) lattice distortions are in good agreement with those found before by neutron diffraction.[13]

Upon annealing, our results show different trends in the development of lattice distortions along the *a*- and *c*-axes and between spines and test plates. In the spine samples, the lattice distortions, $\Delta a/a$, are around 0.05 % up to about 200 °C and then are gradually diminishing to zero (Figure 6C) due to heat-assisted destruction of organic macromolecules.[38] The temperature

dependence of $\Delta c/c$ in spines is more complicated (Figure 6D), revealing a substantial increase between room temperature and 200 °C from 0.03–0.04 up to 0.11–0.13 %, which we relate to the crystallization of ACC. At higher temperatures, relaxation of lattice distortions (practically to zero) due to the combustion of organic macromolecules is observed.

In test plates, both lattice distortions (Figure 6C and D) are practically constant up to about 170 °C. Above 170 °C they increase and reach a maximum at 250 °C due to the crystallization of ACC. At higher temperatures, the lattice distortions decrease, but not down to zero as observed in the other species.

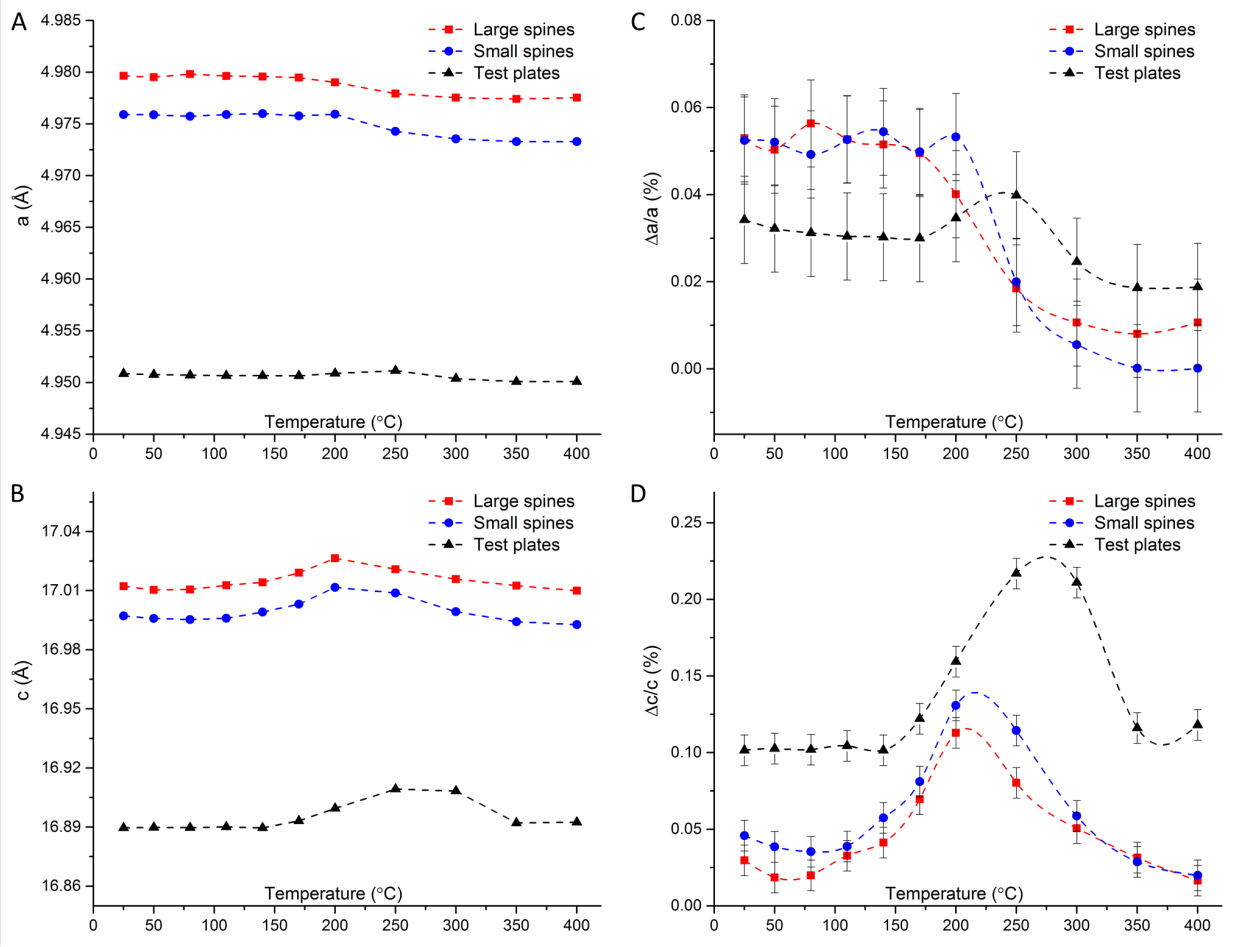

Figure 6: Temperature dependences of: A) lattice parameter, a; B) lattice parameter c; C) lattice distortions, $\Delta a/a$; D) lattice distortions, $\Delta c/c$. Data obtained for large spines, small spines, and test plates are represented, respectively, by red squares, blue dots, and black triangles.

4. DISCUSSION

Biogenic composites, based on calcium carbonate, are complex structures comprising a crystalline part, an amorphous phase, organic macromolecules and some amount of water. The interconnection of these constituents often results in superior properties of the bio-composites. In this paper, we shed additional light on this interconnection in sea urchin skeletal elements by first characterizing the different components and second measuring lattice distortions in the biogenic calcites and their changes induced by heating. The latter approach has been proven to be very effective in the studies of biogenic calcite and aragonite in mollusk shells, as well as in other marine organisms.[38, 65] It is often assumed that lattice distortions arise at an early stage of biomineralization due to the initial deposition of an amorphous precursor and the subsequent amorphous/crystalline phase transformation within confined compartments, outlined by intra-crystalline organics. Crystallization of calcium carbonate is accompanied by the reduction of specific volume per molecule. Therefore, it was suggested that in confined compartments the forces acting at organic/inorganic interfaces will work against this shrinkage, producing relative lattice distortions (strains) primarily of a tensile character.[36] In calcite, the elastic modulus along the a-axis, C_{11} = 149.4 GPa, is much higher than that along the c-axis, C_{33} = 85.2 GPa[66], which implies much smaller effect of equal uniaxial stresses on the a-lattice parameter than on the c-lattice parameter.

In principle, the stress state of a material can also be influenced by pore formation. Additionally to the micron-size pores in sea urchin skeletal parts that are related to the stereom structure (Figure 1), we have experimental results, obtained by small angle X-ray scattering (SAXS), which point out the presence of nano-porosity in our samples. However, temperature-dependent integrated SAXS intensity (see SI Figure 5) is practically constant in the temperature range of ACC crystallization, indicating that the pore volume fraction remains unchanged. In addition, we note that the pore formation in the tensely-stressed material is expected to lead to strain/stress relaxation rather than to strain increase, as we observed during ACC crystallization. Therefore, the observed strain/stress evolution during crystallization is most likely due to atomic interactions at organic/inorganic interfaces rather than pore-assisted mechanism.

In general, we expect that intra-crystalline organic macromolecules influence the amount and type of lattice distortions of the biogenic composites. Furthermore, the magnitude of lattice distortions is affected by the completion of the ACC/calcite phase transformation.[38] In other words, we expect inverse relationship between lattice distortions and the amount of the remnant amorphous phase within the biogenic calcium carbonate. In the following, we discuss the observed lattice distortions behavior upon annealing bearing in mind changes in the content of water, ACC and organics within large and small spines and within the test plates of the sea urchin *P. lividus*. We also further compare these results to those reported for the calcitic prisms of the mollusk shell *P. nobilis*. Using this approach, we expect to better understand the role of organics and ACC in biomineralization processes, in general, and in the origin of lattice distortions in biominerals, in particular.

4.1. ACC and intra-crystalline organics

Using TGA/DSC, HRXRD with internal standard and ^{13}C NMR measurements we evidenced the presence of ACC in the spines and test plates of adult sea urchins. In agreement with ref.,[47] we found about 10 wt. % of ACC in pristine large spines as well as in small spines and test plates. Compared to synthetic ACC and other long-living biogenic ACC (gastrolith),[58, 60] we showed that ACC in sea urchins is less disordered and that the low water content is most likely bound to the ACC phase ($Ca:H_2O$ 1:0.1). Therefore, the ACC in sea urchin skeletal elements is relatively anhydrous in comparison with other long-living biogenic ACCs (e.g. in sponges and ascidians), which are hydrated polymorphs ($Ca:H_2O$ 1:1). Consequently, we suggest that the ACC present in the studied mature skeletal elements of sea urchins is kinetically trapped during biomineralization and is a remnant phase of the two-step reaction that was proposed for sea urchin larval spicule formation ($ACC{\cdot}H_2O \rightarrow ACC \rightarrow$ calcite)[46, 67].

TG-DSC measurements reveal a substantial amount of intra-crystalline organics (1.2 to 1.6 wt.%) in the investigated sea urchin skeletal elements. This value is higher than previously determined (0.1 to 0.2 wt.% of soluble and insoluble fractions) in spines and test plates by biochemical extraction methods.[20, 22] Essential advantage of using TGA for quantifying the total amount of intra-crystalline organics is its insensitivity to the inclusion size or chemistry. For the sake of comparison, substantial amount of organics and water (2.5 wt. %) was measured by TGA in corals[65, 68] and in some calcitic mollusk shells (about 2 wt. %)[69].

In order to further correlate the temperature dependences of lattice distortions to the amount of ACC and intra-crystalline organics in different biogenic calcite samples, we performed additional TGA/DSC measurements with the calcitic prisms of *P. nobilis* mollusk shells. Note, that in *P. nobilis* samples, we did not find clear evidence for an exothermic event that could be

attributed to ACC transformation, as in sea urchin skeletal elements (SI Figure 6A). Furthermore, the weight loss measured in *P. nobilis* by TGA at 820 °C (SI Figure 6B), being put into Eq. (1) together with a Mg content of 2.65 mol.%[13], yielded the intra-crystalline organics fraction equal 0.6 wt.%, which is significantly lower than that obtained for sea urchin skeletal elements.

4.2. Lattice distortions and amorphous phase

The coexistence of calcite, ACC, and organic molecules in sea urchin spines is well-known[23, 47-49], however, the interrelation between these three components still remains unclear.

We argue that the remnant ACC leads to lower initial (before annealing) lattice distortions in sea urchins, as compared with those found in calcitic prims of the mollusk shells of *P. nobilis*. Indeed, in pristine spines we found $\Delta c/c \approx 0.04–0.05$ % and $\Delta c/c \approx 0.1$ % in test samples, i.e. significantly smaller than in *P. nobilis* ($\Delta c/c \approx 0.24$ %) shells.[32] Moreover, in sea urchins we observe a substantial increase of $\Delta c/c$ with annealing temperature up to maximum at temperatures of 200–250 °C (Figure 6D). At these temperatures, the completion of the crystallization process was evidenced by DSC data (Figure 3) that is supported by a substantial decrease of the non-crystalline fraction measured by HRXRD (Figure 5). Interestingly, a slight increase of the *c*-lattice parameter up to a maximum at about 180 °C was also detected upon annealing in *P. nobilis* shell,[32] suggesting a potential presence of a minor ACC amount in there.

The ACC weight fractions in the three types of the sea urchin skeletal elements studied here are nearly equal. Therefore, the differences in the temperature dependences of lattice distortions in the spines and test plates may be related to different types of intra-crystalline organics or their dissimilar spatial distributions, as discussed further below.

4.3. Lattice distortions and intra-crystalline organics

Using TGA/DSC measurements, we found nearly the same amounts of intra-crystalline organics in the three different sea urchin skeletal elements. However, the dTG profiles and DSC/MS measurements suggest that these organic molecules may be of different nature. Although amino acid composition of the protein fraction in sea urchin spines and test plates is very similar,[20, 21] certain dissimilarities have been detected in the spatial distribution of glycoproteins and sialic acid in the dense septa and in the porous stereom of the spines.[24]

Various organic macromolecules, present in the spines and in the test plates, being attached to particular crystallographic planes, will result in different lattice distortions.

Furthermore, differences in the initial lattice distortions between sea urchins and mollusk shells could also be due to the presence of dissimilar organic molecules. Indeed, pristine mollusk shells of *Atrina rigida* and *P. nobilis* shells that show higher $\Delta c/c$ than sea urchin skeletal elements ($\Delta c/c_{(Atrina\ rigida)} \approx 0.19$ % and $\Delta c/c_{(P.\ nobilis)} \approx 0.24$ %)[32], contain proteins that are more acidic [70, 71] than the ones in spines and test plates.[20, 21] It was shown that these acidic proteins strongly interact with the charged calcite planes.[21, 72]

We found that the destruction of organic macromolecules (above 250 °C) in sea urchins skeleton leads to a subsequent reduction of lattice distortions accompanied by the loss of interface coherence,[39] as evidenced by the broadening of X-ray diffraction lines (see SI Figure 7). Note that this broadening effect was observed in other biominerals.[36] Substantial relaxation of lattice distortions upon mild annealing above 250 ºC, when intra-crystalline organics are destroyed, provides strong evidence that lattice distortions are caused by atomic-level interactions at organic/inorganic interfaces. [39] Additional support comes from the fact that

comparable lattice distortions also appear in synthetic calcite grown from solution containing organic macromolecules (see review [38]).

We stress that in spines the magnitude of $\Delta c/c$ decreases almost to zero at 400 °C, while in test plates samples it plateaus at $\Delta c/c \approx 0.11$ %. As evidenced by dTG profile and CO_2 discharge, test plates, as opposed to spines, reveal significant organics destruction at temperatures higher than 400 °C (Figure 2). This means that massive destruction of organic component and corresponding complete relaxation of the lattice distortions is expected at higher temperatures in test plates than in spines.

4.4. Forces acting at the organic/inorganic interfaces

The intra-crystalline organics, together with ACC, are important "ingredients" for producing the lattice distortions measured by HRXRD. Since the amounts of ACC and intra-crystalline organics in the three investigated sea urchin skeletal parts are nearly the same, the differences in the initial values of lattice distortions and their changes upon annealing should be due to distinct interactions between dissimilar intra-crystalline organics and crystallites formed. In order to shed additional light on these distinctions, we converted the measured lattice distortions into the stress tensor components, σ_{11} (in basal plane) and σ_{33} (along the *c*-axis), which arise from the forces acting at the organic/inorganic interfaces.[36] Using known shapes of the strain and stress tensors for hexagonal crystal symmetry, we obtain:

$$\sigma_{11} = (C_{11} + C_{12})\frac{\Delta a}{a} + C_{13}\frac{\Delta c}{c} \qquad (4)$$

$$\sigma_{33} = 2C_{13}\frac{\Delta a}{a} + C_{33}\frac{\Delta c}{c} \qquad (5)$$

where C_{ij} are the components of the calcite stiffness tensor.[73]

The calculated stress components, σ_{11} and σ_{33}, are plotted in Figures 7, as functions of annealing temperature. In general, the temperature dependences of stress components resemble that of lattice distortions (Figures 6). However, a quantitative analysis of these stress functions leads to interesting results. The stress component σ_{33} originates mainly from the action of organic macromolecules attached to the (001) calcite planes, whereas σ_{11} originates from organics attached to the calcite planes parallel to the *c*-axis. For the spines, $\sigma_{33} < \sigma_{11}$ whereas for the test plates, $\sigma_{33} \approx \sigma_{11}$. Therefore, we expect organic molecules to be preferentially attached to the planes parallel to the *c*-axis in the spines and equally attached to planes parallel and perpendicular to the *c*-axis in the test plates. For the sea urchin spines, the stress distribution fits well with earlier observations based on the measurements of the X-ray coherence lengths in sea urchin spines along different crystallographic directions.[23]

Furthermore, we compare the ratio, $\varphi = \sigma_{33}/\sigma_{11}$, for sea urchin elements and for *P. nobilis* prisms (taking the values of lattice distortions from ref.[32]) in the temperature range 25–250 ºC (Figure 7C), i.e. when crystallization of ACC is practically completed. As shown in Figure 7C, the behavior of the stress ratio upon annealing in spines differs from that in test plates and *P. nobilis*. In spines, φ increases up to 1 at 250 ºC (Figure 7C). This suggests that in the remnant ACC regions adjacent to organic macromolecules, the crystallization front proceeds along the *c*-axis. As a result, a part of organic macromolecules become occluded at the (001) atomic planes, subsequently increasing the σ_{33} stress component. This trend, although to a lesser degree, is observed for test plates, evidencing that organics attached to the newly formed (001)-planes is a rather small fraction of those already present at the (001) planes in pristine test samples.

We emphasize that all temperature curves of the ratio, $\varphi = \sigma_{33}/\sigma_{11}$, measured in spines, test plates, and *P. nobilis* shell, converge to $\varphi \approx 1$, when crystallization is completed. In other words,

complete crystallization of ACC within confined space, outlined by organic macromolecules, leads, in these cases, to isotropic distribution of residual stresses, the latter being nearly equal in basal plane of the formed calcite and along the *c*-axis. Further research is needed to understand the molecular mechanisms that stand behind this result.

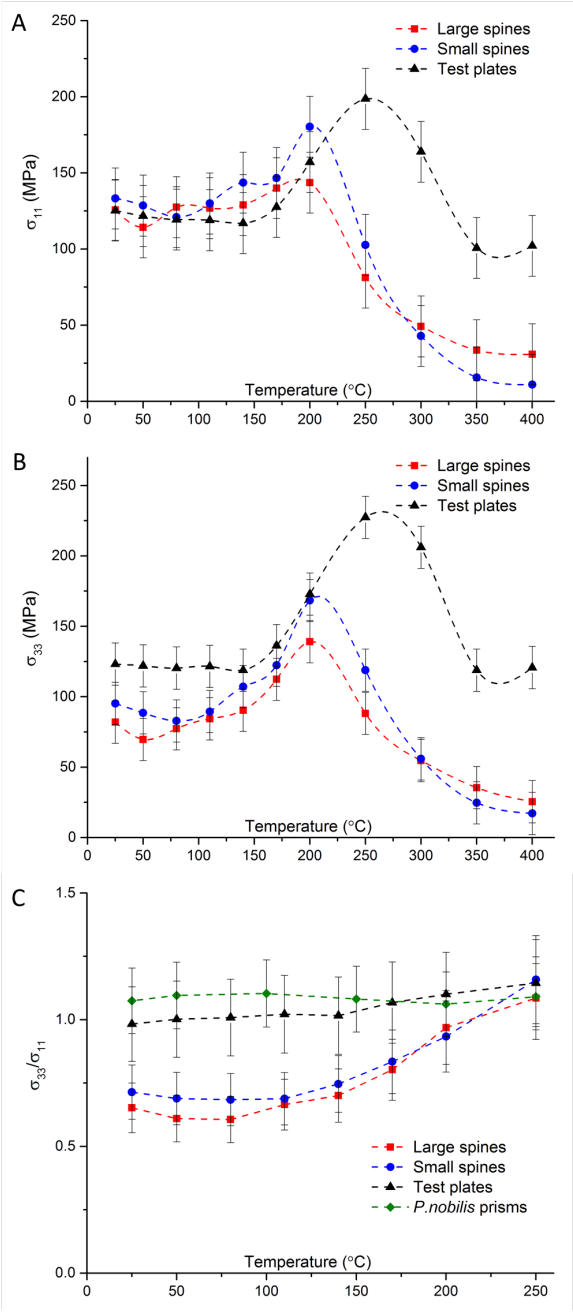

Figure 7: Temperature dependences of: A) the stress component, σ_{11}; B) the stress component, σ_{33}; C) the ratio, $\sigma_{33}/\sigma_{11,}$ converging in all investigated species to $\sigma_{33}/\sigma_{11} \approx 1$ at 250 ºC. Data obtained for large spines, small spines, test plates and *P. nobilis* prisms are represented, respectively, by red squares, blue dots, black triangles and green diamonds.

5. CONCLUSIONS

Using heat treatment and advanced characterization methods, we investigated the interrelationship between calcite, ACC, water, and intra-crystalline organics in skeletal elements of *P. lividus* sea urchins. A significant amount of intra-crystalline organics was found in all pristine samples (average 1.4 wt. %), but different organic molecules are likely present in the spines and test plates. Small amount of water (< 0.2 wt. %) and about 10 wt. % of anhydrous ACC (Ca:H_2O ratio 1:0.1) were detected in all pristine samples. We suggest that this anhydrous ACC is the result of incomplete crystallization during the biomineralization process in adult sea urchins.

As in others biogenic calcites[38], lattice distortions in sea urchin skeletal elements originate from the atomic interactions at organic/inorganic interfaces and are amplified during the crystallization of ACC phase. The latter idea has previously been discussed[13, 38], but never proved experimentally. Here, we provide direct evidence of the amplification mechanism by detecting an increase of lattice distortions (strains) during heat-assisted crystallization of remnant ACC. The strongest effect is on the magnitudes of lattice distortions along the *c*-axis, mostly because the stiffness constant C_{33} in calcite is almost two times smaller than C_{11}.

Using the linear elasticity theory, we convert the measured strains to stress components, acting in the basal plane of calcite (σ_{11}) and along its *c*-axis (σ_{33}). This analysis shows that in pristine

test plates, $\sigma_{33} \approx \sigma_{11}$, while in pristine spines the magnitude of σ_{33} is considerably smaller than that of σ_{11} ($\sigma_{33}/\sigma_{11} \approx 0.7$). Based on these results, we can conclude that in pristine spines and test plates organic macromolecules are preferentially attached to different crystallographic planes of calcite. Crystallization of ACC at about 200-250 ºC leads to the isotropy of residual stresses ($\sigma_{33}/\sigma_{11} \approx 1$) in all types of sea urchin skeletal elements.

Annealing at temperatures above 250 ºC facilitates destruction of intra-crystalline organics and subsequent reduction of lattice distortions. This process is accompanied by considerable broadening of X-ray diffraction lines due to deterioration of the interface quality.

We stress that a rather small amount of ACC (about 10 wt. %) leads to relatively low lattice distortions in pristine sea urchin skeletal parts. Therefore, it is reasonable to assume that relatively thin ACC regions are adjacent to organic/inorganic interfaces, serving as buffer layers between intra-crystalline organics and crystalline calcite. This phenomenon seems to be common in biominerals, which are formed *via* an amorphous precursor and might have functional advantages[74]. This principle resembles the use of amorphous buffer layers in semiconductor heterostructures, grown to prevent large lattice mismatch between components and non-desired dislocation formation. One could further speculate that the degree of crystallization depends on an energy balance between stabilizing an otherwise unstable amorphous phase and forming a crystal with elastic energy stored in the form of lattice strains.

We believe that the results presented here provide strong evidence that the three main components in sea urchin skeletal elements, i.e., ACC, intra-crystalline organics and calcite act in synergy to build bio-composites adapted to appropriate function. This is another astonishing

example of the intricate design of biominerals, which have been evolutionary developed *via* complex biomineralization pathways.

ASSOCIATED CONTENT

Supporting Information. XRD profiles collected from the spine and plate test powders after TGA-DSC measurements. MS measurements of the temperature-dependent release of water vapors and CO_2. Comparison of the ^{13}C MAS NMR and $^{1}H \rightarrow ^{13}C$ CP MAS spectra taken from the large spines and test plates; $^{1}H \rightarrow ^{13}C$ CP MAS spectra with different contact times for the large spines. Typical HRXRD profile measured at ID22. Three tables, containing the results of Rietveld refinement of the HRXRD data taken from large spines, small spines, and test plates. Temperature-dependent total SAXS intensity. TGA-DSC measurements of the prismatic layer of the *P. nobilis* mollusk shell. Temperature dependences of the FWHM of the diffraction profiles for the (300)- and the (006)-reflections. Video of the decrepitation effect between 400 and 450 ^{o}C observed with the powders of large spines and test plates.

AUTHOR INFORMATION

Corresponding Author

*yael.politi@mpikg.mpg.de, marie.alberic@mpikg.mpg.de

Author Contributions

The manuscript was written through contributions of all authors. All authors have given approval to the final version of the manuscript. ‡These authors contributed equally.

Funding Sources

MA is supported by an Alexander von Humboldt postdoctoral fellowship (Ref 3.3-FRA-1163259-HFST-P).

ACKNOWLEDGMENT

We are grateful to Jeannette Steffen from the MPI (Potsdam-Golm) for acquiring the ICP-OES data, to Dr. Dina Shpasser (Technion) for measuring the TGA-MS and Dr. Zhaoyong Zou MPI (Potsdam-Golm) for helping with TGA-DSC measurements. We thank Dr. Igor Zlotnikov (TU Dresden) for providing prismatic layers of *P. nobilis* mollusk shell. We acknowledge the European Synchrotron Radiation Facility (ESRF) for allocating beam times and would like to thank ID22 beam line scientists and local contacts Dr. Wilson Mogodi, Dr. Mauro Coduri, Dr. Carlotta Giacobbe and Dr. Catherine Dejoie for their assistance during beam time. We particularly acknowledge Dr. Andrew Fitch, scientist in charge of ID22 at ESRF, for his help and advices in X-ray diffraction measurements. One of us (EZ) thanks the Shore Fund in Advanced Composites (Technion) for partial financial support.

REFERENCES

(1) Lowenstam, H. A.; Weiner, S., *On Biomineralozation*. ed.; New York, 1989.
(2) Weiner, S.; Addadi, L., Design strategies in mineralized biological materials. *J. Mater. Chem.* **1997,** 7, (5), 689-702.
(3) Addadi, L.; Weiner, S., Biomineralization: mineral formation by organisms. *Phys. Scr.* **2014,** 89, (9), 13.
(4) Meyers, M. A.; Chen, P. Y.; Lin, A. Y. M.; Seki, Y., Biological materials: Structure and mechanical properties. *Prog. Mater. Sci.* **2008,** 53, (1), 1-206.
(5) Espinosa, H. D.; Rim, J. E.; Barthelat, F.; Buehler, M. J., Merger of structure and material in nacre and bone - Perspectives on de novo biomimetic materials. *Prog. Mater. Sci.* **2009,** 54, (8), 1059-1100.
(6) Ji, B. H.; Gao, H. J., Mechanical Principles of Biological Nanocomposites. In *Annual Review of Materials Research*, Clarke, D. R.; Ruhle, M.; Zok, F., Eds. Annual Reviews: Palo Alto, 2010; Vol. 40, pp 77-100.

(7) Dunlop, J. W. C.; Fratzl, P., Biological Composites. In *Annual Review of Materials Research*, Clarke, D. R.; Ruhle, M.; Zok, F., Eds. Annual Reviews: Palo Alto, 2010; Vol. 40, pp 1-24.
(8) Barthelat, F., Architectured materials in engineering and biology: fabrication, structure, mechanics and performance. *Int. Mater. Rev.* **2015,** 60, (8), 413-430.
(9) Aizenberg, J.; Tkachenko, A.; Weiner, S.; Addadi, L.; Hendler, G., Calcitic microlenses as part of the photoreceptor system in brittlestars. *Nature* **2001,** 412, (6849), 819-822.
(10) Heatfield, B. M., Growth of calcareous skeleton during regeneration of spines of sea urchin, strongylocentrotus-purpuratus (stimpson) - light and scanning electron microscopic study. *J. Morphol.* **1971,** 134, (1), 57-90.
(11) Smith, B. A., Stereom microstructure of the echinoid test. *Special Papers in Palaeontology* **1980,** 25, 1-324.
(12) Magdans, U.; Gies, H., Single crystal structure analysis of sea urchin spine calcites: Systematic investigations of the Ca/Mg distribution as a function of habitat of the sea urchin and the sample location in the spine. *Eur. J. Mineral.* **2004,** 16, (2), 261-268.
(13) Zolotoyabko, E.; Caspi, E. N.; Fieramosca, J. S.; Von Dreele, R. B.; Marin, F.; Mor, G.; Addadi, L.; Weiner, S.; Politi, Y., Differences between Bond Lengths in Biogenic and Geological Calcite. *Cryst. Growth Des.* **2010,** 10, (3), 1207-1214.
(14) Politi, Y.; Batchelor, D. R.; Zaslansky, P.; Chmelka, B. F.; Weaver, J. C.; Sagi, I.; Weiner, S.; Addadi, L., Role of Magnesium Ion in the Stabilization of Biogenic Amorphous Calcium Carbonate: A Structure-Function Investigation. *Chem. Mat.* **2010,** 22, (1), 161-166.
(15) Weber, J.; Greer, R.; Voight, B.; White, E.; Roy, R., Unusual strength properties of echinoderm calcite related to structure. *Journal of Ultrastructure Research* **1969,** 26, (5-6), 355-366.
(16) Ma, Y. R.; Aichmayer, B.; Paris, O.; Fratzl, P.; Meibom, A.; Metzler, R. A.; Politi, Y.; Addadi, L.; Gilbert, P.; Weiner, S., The grinding tip of the sea urchin tooth exhibits exquisite control over calcite crystal orientation and Mg distribution. *Proc. Natl. Acad. Sci. U. S. A.* **2009,** 106, (15), 6048-6053.
(17) Veis, A., Organic Matrix-related mineralization of sea urchin spicules, spines, test and teeth. *Front. Biosci.* **2011,** 16, 2540-2560.
(18) Gorzelak, P.; Stolarski, J.; Dubois, P.; Kopp, C.; Meibom, A., (26)mg labeling of the sea urchin regenerating spine: Insights into echinoderm biomineralization process. *J. Struct. Biol.* **2011,** 176, (1), 119-126.
(19) Moureaux, C.; Perez-Huerta, A.; Compere, P.; Zhu, W.; Leloup, T.; Cusack, M.; Dubois, P., Structure, composition and mechanical relations to function in sea urchin spine. *J. Struct. Biol.* **2010,** 170, (1), 41-49.
(20) Weiner, S., Organic matrix-like macromolecules associated with the mineral phase of sea-urchin skeletal plates and teeth. *J. Exp. Zool.* **1985,** 234, (1), 7-15.
(21) Albeck, S.; Aizenberg, J.; Addadi, L.; Weiner, S., Interactions of various skeletal intracrystalline components with calcite crystals. *J. Am. Chem. Soc.* **1993,** 115, (25), 11691-11697.
(22) Kanold, J. M.; Guichard, N.; Immel, F.; Plasseraud, L.; Corneillat, M.; Alcaraz, G.; Brummer, F.; Marin, F., Spine and test skeletal matrices of the Mediterranean sea urchin Arbacia lixula - a comparative characterization of their sugar signature. *Febs J.* **2015,** 282, (10), 1891-1905.

(23) Aizenberg, J.; Hanson, J.; Koetzle, T. F.; Weiner, S.; Addadi, L., Control of macromolecule distribution within synthetic and biogenic single calcite crystals. *J. Am. Chem. Soc.* **1997,** 119, (5), 881-886.
(24) Ameye, L.; De Becker, G.; Killian, C.; Wilt, F.; Kemps, R.; Kuypers, S.; Dubois, P., Proteins and saccharides of the sea urchin organic matrix of mineralization: Characterization and localization in the spine skeleton. *J. Struct. Biol.* **2001,** 134, (1), 56-66.
(25) Goodwin, T. W.; Srisukh, S., A study of the pigments of the sea-urchins, echinus-esculentus l and paracentrotus-lividus lamarck. *Biochem. J.* **1950,** 47, (1), 69-76.
(26) Donnay, G.; Pawson, D. L., X-ray diffraction studies of echinoderm plates. *Science* **1969,** 166, (3909), 1147-1150.
(27) Towe, K. M., Echinoderm calcite - single crystal or polycrystalline aggregate. *Science* **1967,** 157, (3792), 1048-1050.
(28) O'Neill, P. L., Polycrystalline echinoderm calcite and its fracture-mechanics. *Science* **1981,** 213, (4508), 646-648.
(29) Berman, A.; Addadi, L.; Weiner, S., Interactions of sea-urchin skeleton macromolecules with growing calcite crystals - a study of intracrystalline proteins. *Nature* **1988,** 331, (6156), 546-548.
(30) Weber, E.; Pokroy, B., Intracrystalline inclusions within single crystalline hosts: from biomineralization to bio-inspired crystal growth. *Crystengcomm* **2015,** 17, (31), 5873-5883.
(31) Aizenberg, J.; Hanson, J.; Koetzle, T. F.; Leiserowitz, L.; Weiner, S.; Addadi, L., Biologically induced reduction in symmetry - a study of crystal texture of calcitic sponge spicules. *Chem.-Eur. J.* **1995,** 1, (7), 414-422.
(32) Pokroy, B.; Fitch, A. N.; Marin, F.; Kapon, M.; Adir, N.; Zolotoyabko, E., Anisotropic lattice distortions in biogenic calcite induced by intra-crystalline organic molecules. *J. Struct. Biol.* **2006,** 155, (1), 96-103.
(33) Metzger, T. H.; Politi, Y.; Carbone, G.; Bayerlein, B.; Zlotnikov, I.; Zolotoyabko, E.; Fratzl, P., Nanostructure of Biogenic Calcite and Its Modification under Annealing: Study by High-Resolution X-ray Diffraction and Nanoindentation. *Cryst. Growth Des.* **2014,** 14, (10), 5275-5282.
(34) Gilow, C.; Zolotoyabko, E.; Paris, O.; Fratzl, P.; Aichmayer, B., Nanostructure of Biogenic Calcite Crystals: A View by Small-Angle X-Ray Scattering. *Cryst. Growth Des.* **2011,** 11, (6), 2054-2058.
(35) Raup, D. M., Crystallography of echinoid calcite. *J. Geol.* **1959,** 67, (6), 661-674.
(36) Zolotoyabko, E.; Pokroy, B., Biomineralization of calcium carbonate: structural aspects. *Crystengcomm* **2007,** 9, (12), 1156-1161.
(37) Pokroy, B.; Quintana, J. P.; Caspi, E. N.; Berner, A.; Zolotoyabko, E., Anisotropic lattice distortions in biogenic aragonite. *Nat. Mater.* **2004,** 3, (12), 900-902.
(38) Zolotoyabko, E., Anisotropic Lattice Distortions in Biogenic Minerals Originated from Strong Atomic Interactions at Organic/Inorganic Interfaces. *Adv. Mater. Interfaces* **2017,** 4, (1), 1-12.
(39) Pokroy, B.; Fitch, A. N.; Zolotoyabko, E., The microstructure of biogenic calcite: A view by high-resolution synchrotron powder diffraction. *Adv. Mater.* **2006,** 18, (18), 2363-2368.
(40) Addadi, L.; Raz, S.; Weiner, S., Taking advantage of disorder: Amorphous calcium carbonate and its roles in biomineralization. *Adv. Mater.* **2003,** 15, (12), 959-970.
(41) Gower, L. B., Biomimetic Model Systems for Investigating the Amorphous Precursor Pathway and Its Role in Biomineralization. *Chem. Rev.* **2008,** 108, (11), 4551-4627.

(42) Weiner, S.; Addadi, L., Crystallization Pathways in Biomineralization. In *Annual Review of Materials Research*, Clarke, D. R.; Fratzl, P., Eds. Annual Reviews: Palo Alto, 2011; Vol. 41, pp 21-40.
(43) Beniash, E.; Aizenberg, J.; Addadi, L.; Weiner, S., Amorphous calcium carbonate transforms into calcite during sea urchin larval spicule growth. *Proc. R. Soc. B-Biol. Sci.* **1997,** 264, (1380), 461-465.
(44) Aizenberg, J.; Weiner, S.; Addadi, L., Coexistence of amorphous and crystalline calcium carbonate in skeletal tissues. *Connect. Tissue Res.* **2003,** 44, 20-25.
(45) Politi, Y.; Levi-Kalisman, Y.; Raz, S.; Wilt, F.; Addadi, L.; Weiner, S.; Sagi, I., Structural characterization of the transient amorphous calcium carbonate precursor phase in sea urchin embryos. *Adv. Funct. Mater.* **2006,** 16, (10), 1289-1298.
(46) Politi, Y.; Metzler, R. A.; Abrecht, M.; Gilbert, B.; Wilt, F. H.; Sagi, I.; Addadi, L.; Weiner, S.; Gilbert, P., Transformation mechanism of amorphous calcium carbonate into calcite in the sea urchin larval spicule. *Proc. Natl. Acad. Sci. U. S. A.* **2008,** 105, (45), 17362-17366.
(47) Seto, J.; Ma, Y. R.; Davis, S. A.; Meldrum, F.; Gourrier, A.; Kim, Y. Y.; Schilde, U.; Sztucki, M.; Burghammer, M.; Maltsev, S.; Jager, C.; Colfen, H., Structure-property relationships of a biological mesocrystal in the adult sea urchin spine *Proc. Natl. Acad. Sci. U. S. A.* **2012,** 109, (10), 3699-3704.
(48) Politi, Y.; Arad, T.; Klein, E.; Weiner, S.; Addadi, L., Sea urchin spine calcite forms via a transient amorphous calcium carbonate phase. *Science* **2004,** 306, (5699), 1161-1164.
(49) Su, X.; Kamat, S.; Heuer, A. H., The structure of sea urchin spines, large biogenic single crystals of calcite. *J. Mater. Sci.* **2000,** 35, (22), 5545-5551.
(50) Fitch, A. N., The high resolution powder diffraction beam line at ESRF. *J. Res. Natl. Inst. Stand. Technol.* **2004,** 109, (1), 133-142.
(51) Rodriguez Carvajal, J., Recent advances in magnetic-structure determination by neutron powder diffraction. *Physica B* **1993,** 192, (1-2), 55-69.
(52) Hall, D. L.; Bodnar, R. J., Comparison of fluid inclusion decrepitation and acoustic-emission profiles of westerly granite and sioux quartzite. *Tectonophysics* **1989,** 168, (4), 283-296.
(53) Lamar, J. E.; Shrode, R. S., Water soluble salts in limestones and dolomites. *Economic Geology* **1953,** 48, 97-112.
(54) Wardecki, D.; Przenioslo, R.; Brunelli, M., Internal pressure in annealed biogenic aragonite. *Crystengcomm* **2008,** 10, (10), 1450-1453.
(55) Khan, N.; Dollimore, D.; Alexander, K.; Wilburn, F. W., The origin of the exothermic peak in the thermal decomposition of basic magnesium carbonate. *Thermochim. Acta* **2001,** 367, 321-333.
(56) Wolf, S. L. P.; Jahme, K.; Gebauer, D., Synergy of Mg2+ and poly(aspartic acid) in additive-controlled calcium carbonate precipitation. *Crystengcomm* **2015,** 17, (36), 6857-6862.
(57) Radha, A. V.; Forbes, T. Z.; Killian, C. E.; Gilbert, P.; Navrotsky, A., Transformation and crystallization energetics of synthetic and biogenic amorphous calcium carbonate. *Proc. Natl. Acad. Sci. U. S. A.* **2010,** 107, (38), 16438-16443.
(58) Ben Shir, I.; Kababya, S.; Schmidt, A., Molecular-Level Structure-Property Relationships in Biogenic Calcium Carbonates: The Unique Insights of Solid-State NMR Spectroscopy. *Isr. J. Chem.* **2014,** 54, (1-2), 74-85.

(59) Gebauer, D.; Gunawidjaja, P. N.; Ko, J. Y. P.; Bacsik, Z.; Aziz, B.; Liu, L. J.; Hu, Y. F.; Bergstrom, L.; Tai, C. W.; Sham, T. K.; Eden, M.; Hedin, N., Proto-Calcite and Proto-Vaterite in Amorphous Calcium Carbonates. *Angew. Chem.-Int. Edit.* **2010,** 49, (47), 8889-8891.
(60) Akiva-Tal, A.; Kababya, S.; Balazs, Y. S.; Glazer, L.; Berman, A.; Sagi, A.; Schmidt, A., In situ molecular NMR picture of bioavailable calcium stabilized as amorphous $CaCO_3$ biomineral in crayfish gastroliths. *Proc. Natl. Acad. Sci. U. S. A.* **2011,** 108, (36), 14763-14768.
(61) Reeder, R. J.; Tang, Y. Z.; Schmidt, M. P.; Kubista, L. M.; Cowan, D. F.; Phillips, B. L., Characterization of Structure in Biogenic Amorphous Calcium Carbonate: Pair Distribution Function and Nuclear Magnetic Resonance Studies of Lobster Gastrolith. *Cryst. Growth Des.* **2013,** 13, (5), 1905-1914.
(62) Yang, S. Y.; Chang, H. H.; Lin, C. J.; Huang, S. J.; Chan, J. C. C., Is Mg-stabilized amorphous calcium carbonate a homogeneous mixture of amorphous magnesium carbonate and amorphous calcium carbonate? *Chem. Commun.* **2016,** 52, (77), 11527-11530.
(63) Tsai, T. W. T.; Chan, J. C. C., Recent Progress in the Solid-State NMR Studies of Biomineralization. In *Annual Reports on Nmr Spectroscopy, Vol 73*, Webb, G. A., Ed. Elsevier Academic Press Inc: San Diego, 2011; Vol. 73, pp 1-61.
(64) De La Torre, A. G.; Bruque, S.; Aranda, M. A. G., Rietveld quantitative amorphous content analysis. *J. Appl. Crystallogr.* **2001,** 34, 196-202.
(65) Floquet, N.; Vielzeuf, D.; Ferry, D.; Ricolleau, A.; Heresanu, V.; Perrin, J.; Laporte, D.; Fitch, A. N., Thermally Induced Modifications and Phase Transformations of Red Coral Mg-Calcite Skeletons from Infrared Spectroscopy and High Resolution Synchrotron Powder Diffraction Analyses. *Cryst. Growth Des.* **2015,** 15, (8), 3690-3706.
(66) Chen, C. C.; Lin, C. C.; Liu, L. G.; Sinogeikin, S. V.; Bass, J. D., Elasticity of single-crystal calcite and rhodochrosite by Brillouin spectroscopy. *Am. Miner.* **2001,** 86, (11-12), 1525-1529.
(67) Gong, Y. U. T.; Killian, C. E.; Olson, I. C.; Appathurai, N. P.; Amasino, A. L.; Martin, M. C.; Holt, L. J.; Wilt, F. H.; Gilbert, P., Phase transitions in biogenic amorphous calcium carbonate. *Proc. Natl. Acad. Sci. U. S. A.* **2012,** 109, (16), 6088-6093.
(68) Cuif, J. P.; Dauphin, Y.; Berthet, P.; Jegoudez, J., Associated water and organic compounds in coral skeletons: Quantitative thermogravimetry coupled to infrared absorption spectrometry. *Geochem. Geophys. Geosyst.* **2004,** 5, 1-9.
(69) Okumura, T.; Suzuki, M.; Nagasawa, H.; Kogure, T., Microstructural Variation of Biogenic Calcite with Intracrystalline Organic Macromolecules. *Cryst. Growth Des.* **2012,** 12, (1), 224-230.
(70) Weiner, S.; Hood, L., Soluble protein of the organic matrix of mollusk shells: a potential template for shell formation. *Science* **1975,** 190, (4218), 987-989.
(71) Marin, F.; Luquet, G.; Marie, B.; Medakovic, D., Molluscan shell proteins: Primary structure, origin, and evolution. In *Current Topics in Developmental Biology*, Schatten, G. P., Ed. Elsevier Academic Press Inc: San Diego, 2008; Vol. 80, pp 209-276.
(72) Marin, F.; Amons, R.; Guichard, N.; Stigter, M.; Hecker, A.; Luquet, G.; Layrolle, P.; Alcaraz, G.; Riondet, C.; Westbroek, P., Caspartin and calprismin, two proteins of the shell calcitic prisms of the Mediterranean fan mussel Pinna nobilis. *J. Biol. Chem.* **2005,** 280, (40), 33895-33908.
(73) Nye, J. F., *Physical Properties of Crystals*. ed.; Clarendon Press: Oxford, 2001.
(74) Politi, Y.; Weaver, J. C., Built for tough conditions. *Science* **2015,** 347, (6223), 712-713.

For Table of Contents Use Only

The interplay between calcite, amorphous calcium carbonate and intra-crystalline organics in sea urchin skeletal elements

Marie Albéric, Elad N. Caspi, Mathieu Bennet, Widad Ajili, Nadine Nassif, Thierry Azaïs, Alex Berner, Peter Fratzl, Emil Zolotoyabko, Luca Bertinetti, Yael Politi

TABLE OF CONTENT GRAPHICS

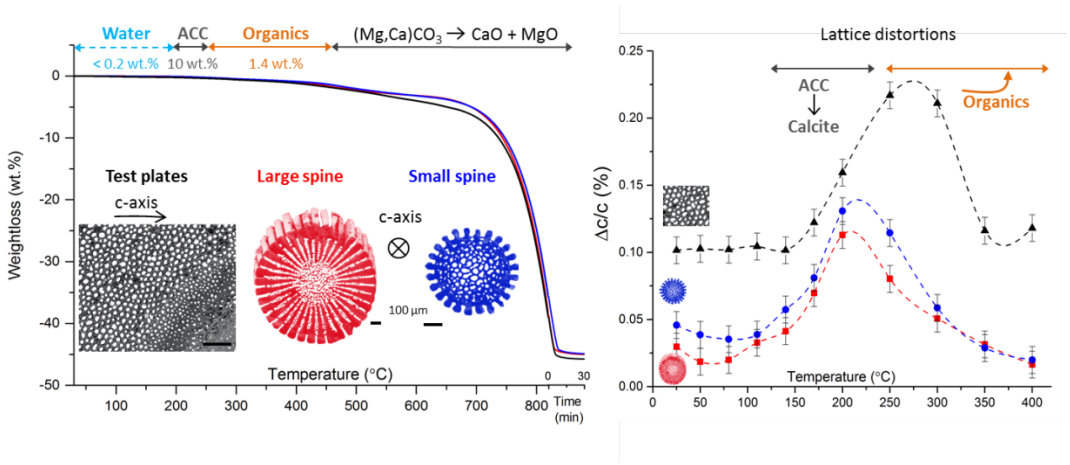

SYNOPSIS

We show that sea urchin spines and test plates are composed of Mg-containing calcite and comprise about 10 wt. % of anhydrous amorphous calcium carbonate (ACC), 1.4 wt. % of organics and less than 0.2 wt. % of water. By following structural and compositional changes in sea urchin skeletal elements upon mild annealing, we uncover the interplay between the constituting components and draw conclusions regarding the biomineralization pathways in adult sea urchin species.